

Two-size approximation: a simple way of treating the evolution of grain size distribution in galaxies

Hiroyuki Hirashita*

Institute of Astronomy and Astrophysics, Academia Sinica, PO Box 23-141, Taipei 10617, Taiwan

2014 December 11

ABSTRACT

Full calculations of the evolution of grain size distribution in galaxies are in general computationally heavy. In this paper, we propose a simple model of dust enrichment in a galaxy with a simplified treatment of grain size distribution by imposing a ‘two-size approximation’; that is, all the grain population is represented by small (grain radius $a < 0.03 \mu\text{m}$) and large ($a > 0.03 \mu\text{m}$) grains. We include in the model dust supply from stellar ejecta, destruction in supernova shocks, dust growth by accretion, grain growth by coagulation and grain disruption by shattering, considering how these processes work on the small and large grains. We show that this simple framework reproduces the main features found in full calculations of grain size distributions as follows. The dust enrichment starts with the supply of large grains from stars. At a metallicity level referred to as the critical metallicity of accretion, the abundance of the small grains formed by shattering becomes large enough to rapidly increase the grain abundance by accretion. Associated with this epoch, the mass ratio of the small grains to the large grains reaches the maximum. After that, this ratio converges to the value determined by the balance between shattering and coagulation, and the dust-to-metal ratio is determined by the balance between accretion and shock destruction. With a Monte Carlo simulation, we demonstrate that the simplicity of our model has an advantage in predicting statistical properties. We also show some applications for predicting observational dust properties such as extinction curves.

Key words: dust, extinction — galaxies: evolution — galaxies: ISM — methods: analytical

1 INTRODUCTION

Dust enrichment has a large impact on the evolution of galaxies in various aspects. Dust grains induce the formation of molecular gas through dust surface reaction of some molecular species, especially H_2 (e.g. Gould and Salpeter 1963; Hirashita & Ferrara 2002; Cazaux & Tielens 2004). Dust also affects the typical stellar mass or the initial mass function (IMF) (Schneider et al. 2006) as dust cooling induces fragmentation of molecular clouds (Omukai 2000; Omukai et al. 2005). Moreover, dust grains absorb optical and ultraviolet (UV) stellar light and reprocess it into infrared bands, dramatically affecting the observed galaxy spectral energy distributions (SEDs) (e.g. Takeuchi et al. 2005). The efficiencies of the above processes are mostly proportional to the total dust amount (or abundance) in the system.

Besides the total dust amount, dust properties constitute another important aspect in dust evolution. Among them, the grain size distribution is of particular importance since the optical properties such as extinction curves and grain-surface chemical reaction rates are directly modified if the grain size distribution changes. In

other words, even if we precisely modeled the evolution of total dust amount in a system, lack of knowledge of the grain size distribution would cause large uncertainties in optical and chemical characteristics of the system. Moreover, as shown below, the grain size distribution also affects the evolution of the total dust amount (see also Kuo & Hirashita 2012). Therefore, it is crucial to model the total dust amount and the dust properties (especially the grain size distribution) at the same time.

Recently Asano et al. (2013a, hereafter A13) have constructed a full framework of treating the evolution of grain size distribution over the entire galaxy evolution. Their calculations suggest the following evolutionary features of grain size distribution. At the early stage of galaxy evolution, when the system is metal-poor, the dust is predominantly supplied from core-collapse supernovae (simply referred to as SNe) and asymptotic giant branch (AGB) stars. If the system reaches a metallicity level referred to as the critical metallicity, shattering produces a large amount of small grains, which eventually grow by accreting gas-phase metals in the dense interstellar medium (ISM). This accretion becomes the dominant mechanism of grain mass increase at metallicities beyond the critical metallicity. After that, coagulation in dense clouds pushes the small grains towards larger sizes. The evolution of extinction curves is

* E-mail: hirashita@asiaa.sinica.edu.tw

also investigated by Asano et al. (2014) using the evolution models of grain size distribution in A13.

The importance of including dust in cosmological galaxy evolution models has been shown by many authors. Among them, Dayal, Hirashita, & Ferrara (2010) included dust production and destruction in a cosmological simulation, predicting the statistical properties of dust emission luminosities in a large sample of high-redshift galaxies. More elaborate dust evolution models that include two major dust formation mechanisms (dust formation in stellar ejecta and dust growth by accretion in the ISM) are also incorporated in semi-analytic (Valiante et al. 2011; de Bressan et al. 2014) or N -body (Bekki 2013; Yozin & Bekki 2014) frameworks.

However, the above cosmological galaxy evolution models only take the total dust content into account. It still remains challenging to include grain size distributions in these frameworks, because the freedom of grain size adds another dimension to the calculations. In fact, Yajima et al. (2014) show that the extinction properties of Lyman-break galaxies are influenced by the assumed dust size. At the same time, as shown by A13 (see above), the evolution of the total dust amount is coupled with that of the grain size distribution. Therefore, it is desirable to develop a method of treating the information on grain size distribution in a computationally light manner.

The first purpose of this paper is to develop a simple and light method of treating the evolution of grain size distribution in a galaxy. Such a ‘light’ method is also useful to analyze the dependence on various parameters that govern the grain size distribution, since we can easily run numerous cases with different parameter values. Thus, the second purpose of this paper is detailed analysis of the response of dust enrichment to various dust enrichment and processing mechanisms. We also address future prospect of including the light dust evolution model developed in this paper into such complex galaxy evolution models as mentioned above (i.e. semi-analytic models, N -body simulations, etc.).

In this paper, we first review the dust enrichment and processing mechanisms in Section 2.1, where we note that most of the dust formation and processing mechanisms work distinctively on small ($\lesssim 0.03 \mu\text{m}$) grains and large ($\gtrsim 0.03 \mu\text{m}$) grains. This motivates us to apply a ‘two-size approximation’, in which we represent the grain size distribution by the ratio of the total mass of the small grains to that of the large grains. This ratio is referred to as the ‘small-to-large grain abundance ratio’. As demonstrated in this paper, this ‘two-size approximation’ nicely catches the features in the full calculations of grain size evolution. We also propose to use this two-size approximation in complex galaxy evolution models.

The paper is organized as follows: we review the processes to be taken into account, and formulate the model by using the two-size approximation in Section 2. We show the results in Section 3. We analyze and discuss the results in Section 4 and consider possibilities of including our models in complex galaxy evolution models in Section 5. Finally we conclude in Section 6.

2 MODEL

2.1 Review of the processes

In considering the evolution of dust in the ISM of a galaxy, we need to consider not only the dust supply from stars but also dust processing in the ISM. Following A13, we include the following processes considered to dominate the evolution of dust content and grain size distribution: (i) dust supply from stellar ejecta, (ii)

Table 1. Processes considered in this paper.

Process ^a	Small Grains ^b	Large Grains ^b	Total
Stellar ejecta	Δ	\nearrow	\nearrow
Shock destruction	\searrow	\searrow	\searrow
Accretion	\nearrow	Δ	\nearrow
Coagulation	\searrow	\nearrow	\rightarrow
Shattering	\nearrow	\searrow	\rightarrow

Note: \nearrow , \searrow , and \rightarrow indicate that the process increases, decreases, and keeps constant the dust mass, respectively. Δ means that the process has little influence on the dust mass.

^aEach process is described in Section 2.1.

^bThe large and small grains are divided at $a \sim 0.03 \mu\text{m}$.

dust destruction in the ISM by supernova (SN) shocks, (iii) grain growth by the accretion of gas-phase metals, (iv) grain growth by coagulation (sticking of grains), and (v) shattering (grain disruption/fragmentation). These processes act differently on large and small grains. Here we roughly divide the grains into large and small grains at $a \sim 0.03 \mu\text{m}$, where a is the grain radius. We hereafter refer to grains with $a > 0.03 \mu\text{m}$ and $a < 0.03 \mu\text{m}$ as the large grains and the small grains, respectively. We summarize these processes in Table 1. We also show, based on A13, how each process acts on different grain sizes. We explain each process in what follows.

The dominant stellar sources of dust are SNe and AGB stars (Gall et al. 2011, for a review), and both types of sources are predicted to supply large grains. The dust supplied from SNe tends to be biased to large sizes because reverse shock destruction is more effective for small grains than large ones (Nozawa et al. 2007; see also Bianchi & Schneider 2007). The typical size of grains produced by AGB stars is also suggested to be large ($a \gtrsim 0.1 \mu\text{m}$) from observations of SEDs (Groenewegen 1997; Gauger et al. 1999), although Hofmann et al. (2001) showed that the grains are not single-sized. Theoretical studies have also shown that large ($\gtrsim 0.1 \mu\text{m}$) dust grains form in the winds of AGB stars (Winters et al. 1997; Yasuda & Kozasa 2012; Ventura et al. 2012). There are also pieces of evidence obtained by meteoritic samples that dust species such as SiC thought to originate from AGB stars from isotopic compositions (Hoppe et al. 1994; Daulton et al. 2003) have large grain sizes ($a \gtrsim 0.1 \mu\text{m}$), supporting the formation of large grains in AGB stars (Amari et al. 1994; Hoppe & Zinner 2000).

Dust grains, after being injected into the ISM, are destroyed by sputtering if they are swept by SN shocks (Dwek & Scalco 1980; McKee 1989). Because thermal sputtering is a surface process (a process whose rate is proportional to the total surface area), the dust destruction time-scale by this process is proportional to the grain radius (Draine & Salpeter 1979). Nonthermal sputtering has little dependence on the grain size (Jones et al. 1996). In essence, for sputtering, it is difficult to separate large and small grains, since ‘large’ grains being destroyed enter the small regime. Therefore, to simplify the treatment and to minimize the number of parameters, we apply the same time-scale of destruction both for the large and the small grains unless otherwise stated. We also examine the case in which the small grains are more efficiently destroyed.

Another important dust formation process is grain growth by the accretion of gas-phase metals in the dense ISM (Dwek 1998; Hirashita 1999; Zhukovska, Gail, & Tieloff 2008; Draine 2009; Inoue 2011; Pipino et al. 2011; Asano et al. 2013b). This process is simply referred to as accretion in this paper. Including accretion into dust evolution models is motivated not only to

explain the dust abundance in nearby galaxies (Hirashita 1999; Inoue 2011; Zhukovska & Henning 2013; de Bressan et al. 2014; Schneider et al. 2014), but also to explain the observations of huge amounts of dust ($\sim 10^8 M_\odot$) in high- z quasars and starbursts (Michałowski et al. 2010; Mattsson 2011; Valiante et al. 2011; Kuo & Hirashita 2012; Rowlands et al. 2014; Nozawa et al. 2015). Grain growth by accretion occurs efficiently only after the ISM is significantly enriched with dust and metals, since the grain growth rate is proportional to the collision rate between these two components. Since the small grains have much larger surface-to-volume ratios than the large grains, accretion has a predominant influence on the small grains, creating a bump in the grain size distribution at $a < 0.03 \mu\text{m}$ (Hirashita & Kuo 2011; Hirashita 2012). The grain size distribution is hardly changed by accretion at $a > 0.03 \mu\text{m}$.

Coagulation occurs in the dense ISM and pushes the grain size distribution toward larger grain sizes (e.g. Ormel et al. 2009; Hirashita & Voshchinnikov 2014). In particular, coagulation is a unique mechanism that converts small grains to large grains, since another grain growth mechanism, accretion, cannot increase the grain radius drastically as mentioned above. Since coagulation converts small grains to large grains, it can be regarded as a destruction mechanism for the small grains and as a formation mechanism for the large grains.

Shattering occurs predominantly in the diffuse ISM (Yan, Lazarian, & Draine 2004; Hirashita & Yan 2009) and in SN shocks (Jones et al. 1996), and creates a large number of small grains from large grains. Shattering is the most efficient mechanism of producing small grains since the fragmentation associated with shattering produce a large number of small grains. Shattering can be regarded as a destruction mechanism for the large grains and as a formation mechanism for the small grains.

2.2 Evolution of small and large grains

We include the above processes in a simple evolution model of dust enrichment in a galaxy. The purpose of our model is to construct a light and simple evolution model of dust amount and grain size, which can be easily included in computationally heavy frameworks of galaxy evolution such as N -body and/or smoothed particle hydrodynamics (SPH) simulations and semi-analytic models. Therefore, we keep our model in this paper as simple as possible by adopting a one-zone closed-box model described in Hirashita & Kuo (2011), although extension of our framework to more elaborate treatments is straightforward (Dwek 1998; Lisenfeld & Ferrara 1998).

The model treats the evolutions of the total gas, metal and dust masses (M_g , M_Z and M_d , respectively) in the galaxy. In this model, the metals include not only gas phase elements but also dust. M_g includes M_Z and M_d , but $M_g \gg M_Z$ and M_d in any case. We newly divide the dust component into the small and large grains (Section 2.1), whose total masses are denoted as $M_{d,s}$ and $M_{d,l}$, respectively. Considering the processes described in Section 2.1 and listed in Table 1, the equations are written as

$$\frac{dM_g}{dt} = -\psi + E, \quad (1)$$

$$\frac{dM_Z}{dt} = -Z\psi + E_Z \quad (2)$$

$$\frac{dM_{d,s}}{dt} = -\mathcal{D}_s\psi - \frac{M_{d,s}}{\alpha\tau_{\text{SN}}} + \frac{M_{d,l}}{\tau_{\text{sh}}} - \frac{M_{d,s}}{\tau_{\text{co}}} + \frac{M_{d,s}}{\tau_{\text{acc}}}, \quad (3)$$

$$\frac{dM_{d,l}}{dt} = -\mathcal{D}_l\psi + f_{\text{in}}E_Z - \frac{M_{d,l}}{\tau_{\text{SN}}} - \frac{M_{d,l}}{\tau_{\text{sh}}} + \frac{M_{d,s}}{\tau_{\text{co}}}, \quad (4)$$

where ψ is the star formation rate, E and E_Z are the rates of the total injection of mass (gas + dust) and metal mass from stars, respectively, and f_{in} is the dust condensation efficiency of the metals in the stellar ejecta. The time-scales of various processes are also introduced: τ_{SN} is the time-scale of dust destruction by SN shocks for the large grains, and $\alpha\tau_{\text{SN}}$ is that for the small grains (i.e. $\alpha \leq 1$ is introduced to consider a possible short destruction time for small grains; Section 2.1; Nozawa et al. 2006); τ_{sh} , τ_{co} , and τ_{acc} are the time-scales of shattering, coagulation, and accretion, respectively. We also define the metallicity, $Z \equiv M_Z/M_g$, the small-grain dust-to-gas ratio, $\mathcal{D}_s \equiv M_{d,s}/M_g$, the large-grain dust-to-gas ratio, $\mathcal{D}_l \equiv M_{d,l}/M_g$, and the dust-to-gas ratio, $\mathcal{D} \equiv \mathcal{D}_{d,s} + \mathcal{D}_{d,l}$.

In order to allow a simple analytical treatment, we adopt the instantaneous recycling approximation; that is, a star with $m > m_t$ (m is the zero-age stellar mass, and m_t is the turn-off mass at fixed age t) dies instantaneously after its birth, leaving a remnant of mass w_m (Tinsley 1980). Once the initial mass function (IMF) is fixed, the returned fraction of the mass from formed stars, \mathcal{R} , and the mass fraction of metals that is newly produced and ejected by stars, \mathcal{Y}_Z , are evaluated. Using these quantities, we write

$$E = \mathcal{R}\psi, \quad (5)$$

$$E_Z = (\mathcal{R}Z + \mathcal{Y}_Z)\psi. \quad (6)$$

For the time-scale of large grain destruction by SN shocks, we define a parameter, $\beta_{\text{SN}} \equiv \tau_{\text{SF}}/\tau_{\text{SN}}$, where $\tau_{\text{SF}} \equiv M_g/\psi$ is the star formation time-scale (treated as a constant for simplicity in this paper) and $\tau_{\text{SN}} = M_g/(\epsilon_{\text{sw},l}M_{\text{sw}}\gamma)$ ($\epsilon_{\text{sw},l}$ and M_{sw} are the dust destruction efficiency and the gas mass swept by a single high-velocity SN blast, respectively, and γ is the SN rate). With the above definitions, $\beta_{\text{SN}} = \epsilon_{\text{sw},l}M_{\text{sw}}\gamma/\psi$, which is treated as a constant with the instantaneous recycling approximation (Hirashita & Kuo 2011).

The time-scales of shattering and coagulation depend on the dust-to-gas ratio, since these processes become efficient as the system is enriched with dust. In our models, we consider shattering of the large grains into the small grains and coagulation of the small grains into the large grains, assuming the following dependences for these two time-scales:

$$\tau_{\text{sh}} = \tau_{\text{sh},0} \left(\frac{\mathcal{D}_l}{\mathcal{D}_{\text{MW},l}} \right)^{-1}, \quad (7)$$

$$\tau_{\text{co}} = \tau_{\text{co},0} \left(\frac{\mathcal{D}_s}{\mathcal{D}_{\text{MW},s}} \right)^{-1}, \quad (8)$$

where we normalize the time-scales to the values ($\tau_{\text{sh},0}$ and $\tau_{\text{co},0}$) at the Milky Way dust-to-gas ratios and the total Milky Way dust-to-gas ratio, 0.01, is divided into the large-grain dust-to-gas ratio ($\mathcal{D}_{\text{MW},l} = 0.0070$) and the small-grain dust-to-gas ratio ($\mathcal{D}_{\text{MW},s} = 0.0030$) assuming the power-law grain size distribution ($\propto a^{-3.5}$) in the grain size ranges 0.001–0.25 μm , which is applicable for the Milky Way dust (Mathis, Rumpl, & Nordsieck 1977, hereafter MRN). For shattering and coagulation, we define β_{sh} and β_{co} in similar ways to β_{SN} above: $\beta_{\text{sh}} \equiv \tau_{\text{SF}}/\tau_{\text{sh}}$ and $\beta_{\text{co}} \equiv \tau_{\text{SF}}/\tau_{\text{co}}$. Note that β_{sh} and β_{co} varies in proportion to \mathcal{D}_l and \mathcal{D}_s , respectively, while β_{SN} is treated as a constant.

For accretion, we adopt the formulation developed by Hirashita & Kuo (2011), who also considered the dependence on grain size distribution. The increasing rate of dust mass by accre-

4 Hirashita

tion is expressed as

$$\frac{M_{d,s}}{\tau_{\text{acc}}} = \frac{\mathcal{B}X_{\text{cl}}M_{d,s}}{\tau_{\text{cl}}}, \quad (9)$$

where we introduce the accretion time-scale, τ_{acc} , X_{cl} is the cold cloud fraction to the total gas mass, τ_{cl} is the lifetime of the cold clouds, and \mathcal{B} is the increment of dust mass in the cold clouds¹, which can be estimated as

$$\mathcal{B} \simeq \left[\frac{\langle a^3 \rangle_0}{3y\langle a^2 \rangle_0 + 3y^2\langle a \rangle_0 + y^3} + \frac{\mathcal{D}_s}{Z - \mathcal{D}} \right]^{-1}, \quad (10)$$

where $y \equiv a_0\xi\tau_{\text{cl}}/\tau$ (a_0 is just used for normalization, ξ is the fraction of metals in gas phase, and τ is the accretion time-scale for a grain with radius a_0), and $\langle a^\ell \rangle_0$ is the ℓ th moment of grain radius. The term $\mathcal{D}_s/(Z - \mathcal{D})$ is based on the fact that \mathcal{B} cannot be larger than the case in which all the gas-phase metals are used up (i.e. $\mathcal{B} < (Z - \mathcal{D})/\mathcal{D}_s$). Here we implicitly assume that the accretion rate in the cold clouds is not affected by other grain processing mechanisms. In fact, coagulation also occurs there, but Hirashita (2012) showed that coagulation does not alter the dust mass growth rate by accretion (or \mathcal{B}). We adopt the following expression for τ (see eq. 23 of Hirashita & Kuo 2011, applicable for silicate, but carbonaceous dust has a similar time-scale):

$$\tau = 6.3 \times 10^7 \left(\frac{Z}{Z_\odot} \right)^{-1} a_{0.1} n_3^{-1} T_{50}^{-1/2} S_{0.3}^{-1} \text{ yr}, \quad (11)$$

where $a_{0.1} \equiv a_0/(0.1 \mu\text{m})$, $n_3 \equiv n_{\text{H}}/(10^3 \text{ cm}^{-3})$ (n_{H} is the number density of hydrogen nuclei in the cold clouds), $T_{50} \equiv T_{\text{gas}}/(50 \text{ K})$ (T_{gas} is the gas temperature), and $S_{0.3} \equiv S/0.3$ (S is the sticking probability of the dust-composing material onto the preexisting grains). We use the same values as in Hirashita & Kuo (2011); i.e. $a_0 = 0.1 \mu\text{m}$, $n_{\text{H}} = 10^3 \text{ cm}^{-3}$, $T_{\text{gas}} = 50 \text{ K}$, and $S = 0.3$. Assuming that the cold clouds hosting accretion and star formation are the same, we can express the star formation rate as

$$\frac{M_{\text{g}}}{\tau_{\text{SF}}} = \frac{\epsilon X_{\text{cl}} M_{\text{g}}}{\tau_{\text{cl}}}, \quad (12)$$

where ϵ is the star formation efficiency of the cold clouds. We define $\beta_{\text{acc}} \equiv \tau_{\text{SF}}/\tau_{\text{acc}}$, which by using equations (9) and (12) can be evaluated as

$$\beta_{\text{acc}} = \frac{\mathcal{B}}{\epsilon}. \quad (13)$$

Equations (1)–(4) are converted to the time evolution of the metallicity $Z = M_{\text{Z}}/M_{\text{g}}$, the small-grain dust-to-gas ratio $\mathcal{D}_s = M_{d,s}/M_{\text{g}}$, and the large-grain dust-to-gas ratio $\mathcal{D}_1 = M_{d,1}/M_{\text{g}}$ as

$$\frac{M_{\text{g}}}{\psi} \frac{dZ}{dt} = \mathcal{Y}_Z, \quad (14)$$

$$\frac{M_{\text{g}}}{\psi} \frac{d\mathcal{D}_1}{dt} = f_{\text{in}}(\mathcal{R}Z + \mathcal{Y}_Z) + \beta_{\text{co}}\mathcal{D}_s - (\beta_{\text{SN}} + \beta_{\text{sh}} + \mathcal{R})\mathcal{D}_1, \quad (15)$$

$$\frac{M_{\text{g}}}{\psi} \frac{d\mathcal{D}_s}{dt} = \beta_{\text{sh}}\mathcal{D}_1 - \left(\frac{\beta_{\text{SN}}}{\alpha} + \beta_{\text{co}} + \mathcal{R} - \beta_{\text{acc}} \right) \mathcal{D}_s. \quad (16)$$

By rearranging equations (14)–(16), we obtain

$$\mathcal{Y}_Z \frac{d\mathcal{D}_1}{dZ} = f_{\text{in}}(\mathcal{R}Z + \mathcal{Y}_Z) + \beta_{\text{co}}\mathcal{D}_s - (\beta_{\text{SN}} + \beta_{\text{sh}} + \mathcal{R})\mathcal{D}_1, \quad (17)$$

¹ Hirashita & Kuo (2011) used the notation β for \mathcal{B} . In order to avoid confusion with β_{acc} introduced later, we use \mathcal{B} in this paper.

$$\mathcal{Y}_Z \frac{d\mathcal{D}_s}{dZ} = \beta_{\text{sh}}\mathcal{D}_1 - \left(\frac{\beta_{\text{SN}}}{\alpha} + \beta_{\text{co}} + \mathcal{R} - \beta_{\text{acc}} \right) \mathcal{D}_s. \quad (18)$$

These two equations are solved to obtain the \mathcal{D}_1 – Z and \mathcal{D}_s – Z relations. If we add Equations (17) and (18), we obtain the evolution of total dust-to-gas ratio, $\mathcal{D} = \mathcal{D}_1 + \mathcal{D}_s$, as

$$\mathcal{Y}_Z \frac{d\mathcal{D}}{dZ} = f_{\text{in}}(\mathcal{R}Z + \mathcal{Y}_Z) - (\beta'_{\text{SN}} + \mathcal{R})\mathcal{D} + \beta_{\text{acc}}\mathcal{D}_s, \quad (19)$$

where $\beta'_{\text{SN}} \equiv \beta_{\text{SN}}(\mathcal{D}_1 + \mathcal{D}_s/\alpha)/\mathcal{D}$ (if $\alpha = 1$, $\beta'_{\text{SN}} = \beta_{\text{SN}}$). Equation (19) is a similar equation to eq. (48) of Hirashita & Kuo (2011) except that the mass increase by accretion is only considered for the small grains in the current paper. The processes that conserve the total dust mass, that is, coagulation and shattering, do not explicitly appear in the evolution of \mathcal{D} , but implicitly affect the evolution of \mathcal{D}_s in the last term.

2.3 Choice of parameter values

As mentioned in the beginning of Section 2.1, we set the boundary of the small and large grains at $a = 0.03 \mu\text{m}$. Indeed, this value can be justified by A13's full calculation of grain size distribution: in their fig. 6 (left panel), the processes dominating the abundance of small grains (accretion, coagulation, and shattering) create a bump in the size distribution at small grain sizes. At large grain sizes, there is another bump created by the dust production by stars. The boundary of these two bumps are around $a \simeq 0.03 \mu\text{m}$, representing the different processes between small and large grains for the evolution of grain size distribution. Therefore, we adopt $a = 0.03 \mu\text{m}$ for the boundary. For accretion, we need to assume a grain size distribution to evaluate the moments of grain radius in equation (10). We assume the MRN grain size distribution ($\propto a^{-3.5}$) between $a = 0.001$ and $0.03 \mu\text{m}$ for the small grains, obtaining $\langle a \rangle_0 = 1.66 \times 10^{-3} \mu\text{m}$, $\langle a^2 \rangle_0^{1/2} = 2.02 \times 10^{-3} \mu\text{m}$, and $\langle a^3 \rangle_0^{1/3} = 2.82 \times 10^{-3} \mu\text{m}$. For accretion, the 'volume-to-surface ratio', $\langle a^3 \rangle_0/\langle a^2 \rangle_0 = 5.48 \times 10^{-3} \mu\text{m}$ is the most important quantity, and this value is near to the bump created by accretion (A13), which confirms the validity of the moments that we adopted.

We adopt $\mathcal{R} = 0.25$ and $\mathcal{Y}_Z = 0.013$ (Hirashita & Kuo 2011; Kuo, Hirashita, & Zafar 2013) under a Salpeter IMF with a stellar mass range of 0.1–100 M_\odot and the instantaneous recycling for $t = 5 \text{ Gyr}$. Although we can change the values of these parameters by adopting a different IMF, etc., we fix them, since they have only a minor influence on the relation between dust-to-gas ratio and metallicity compared with the values of f_{in} and parameters related to accretion.

For the fiducial case, we choose $\tau_{\text{SF}} = 5 \text{ Gyr}$, which is roughly appropriate for nearby spiral galaxies (we also examine $\tau_{\text{SF}} = 0.5$ and 50 Gyr). Since we treat τ_{SF} as a constant, we cannot include the effects of episodic star formation, which may enhance the scatter of the relation between dust-to-gas ratio and metallicity (Zhukovska 2014). For f_{in} , we adopt $f_{\text{in}} = 0.1$ following Inoue (2011), but we also apply their lower efficiency case, $f_{\text{in}} = 0.01$. We adopt $\beta_{\text{SN}} = 9.65$ following Hirashita & Kuo (2011). We also vary β_{SN} by a factor of 2. Such a factor 2 variation is expected by considering inhomogeneity or multi-phase structures in the ISM (McKee 1989). Jones & Nuth (2011) pointed out that the estimate of τ_{SN} is uncertain; however, as shown later, our choice of β_{SN} nicely explains the dust-to-metal ratio of the Milky Way (Section 4.2). For the destruction of small grains, we conservatively choose $\alpha = 1$, but later we will also discuss the cases with $\alpha < 1$. As noted above, $\beta_{\text{SN}} = \tau_{\text{SF}}/\tau_{\text{SN}}$ can be treated as a constant under the instantaneous recycling approximation.

Table 2. Parameter ranges surveyed.

Parameter	Process	Minimum	Maximum	Fiducial
f_{in}	stellar ejecta	0.01	0.1	0.1
β_{SN}	SN destruction	4.8	19	9.65
τ_{cl}	accretion	10^6 yr	10^8 yr	10^7 yr
$\tau_{\text{sh},0}$	shattering	10^7 yr	10^9 yr	10^8 yr
$\tau_{\text{co},0}$	coagulation	10^6 yr	10^8 yr	10^7 yr
τ_{SF}	star formation	0.5 Gyr	50 Gyr	5 Gyr

Accretion is regulated by $\beta_{\text{acc}} = \mathcal{B}/\epsilon$ in equation (10), which is parameterized by the cloud lifetime τ_{cl} and star formation efficiency ϵ . Because of the degeneracy, we only explore variations of the parameter τ_{cl} with fixed values of the other parameters in \mathcal{B} : as we observe in equation (10), a large/small value of τ_{cl} indicates efficient/inefficient accretion; this is because the lifetime of a cloud hosting accretion regulates the duration of accretion there. We adopt $\tau_{\text{cl}} = 10^7$ yr for the fiducial value (Hirashita & Kuo 2011) with an order of magnitude variation also investigated. For the star formation efficiency in the cold clouds, we adopt $\epsilon = 0.1$.

Seok, Hirashita, & Asano (2014) derived shattering and coagulation time-scales in their application of PAH formation and destruction, and we apply approximately the same values for the time-scales for the fiducial case; that is, we adopt $\tau_{\text{sh},0} = 10^8$ yr and $\tau_{\text{co},0} = 10^7$ yr for the fiducial case. Since we expect large variations for both parameters depending on the ISM density and the fractions of various ISM phases (A13), we consider an order of magnitude variations for them.

The above choice of the parameters are summarized in Table 2. For the normalization of metallicity, we adopt the same solar metallicity $Z_{\odot} = 0.02$ as adopted in A13 (originally from Anders & Grevesse 1989).

3 RESULTS

3.1 Relation between dust-to-gas ratio and metallicity

We now show in Fig. 1 the evolution of \mathcal{D}_1 , \mathcal{D}_s , and $\mathcal{D}(= \mathcal{D}_1 + \mathcal{D}_s)$ as a function of Z , calculated by equations (17) and (18). At low metallicity, the large grains dominate the total dust abundance because the stellar dust production is the dominant dust formation mechanism. Since we assume a constant condensation efficiency (f_{in}) of the metals in stellar ejecta, the dust-to-gas ratio is proportional to the metallicity ($\mathcal{D} \simeq \mathcal{D}_1 \simeq f_{\text{in}}Z$) at low metallicity (see also Section 4.1). The slowdown of the increase around $Z \sim 0.1 Z_{\odot}$ is due to the destruction by SN shocks. At the same time, the small grains increase because shattering time-scale becomes short enough to produce small grains through the collisions of the large grains. After that, accretion further accelerates the increase of the small grains, and at the same time, the large grains rapidly increase because coagulation of small grains becomes active. This rapid increase of both small and large grain abundances appears around $Z \sim 0.2 Z_{\odot}$. This increase slows down after a significant fraction of gas-phase metals are used up. The increase of dust-to-gas ratio is driven by the metal enrichment at high metallicity, where the dust-to-metal ratio is determined by the balance between accretion and SN destruction. The small-to-large grain abundance ratio is determined by the balance between shattering and coagulation. See Section 4.2 for quantitative discussions for the high-metallicity regime.

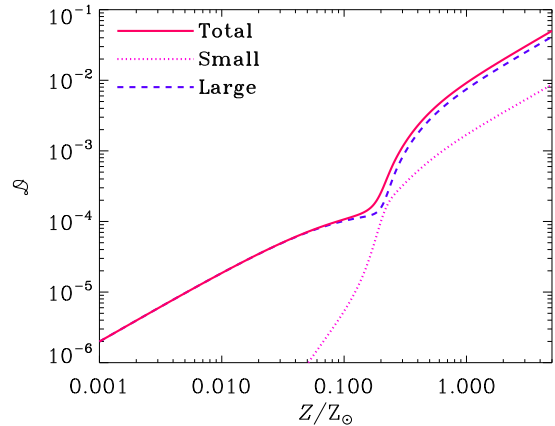


Figure 1. Evolution of dust-to-gas ratio as a function of metallicity Z normalized to the solar metallicity $Z_{\odot} = 0.02$ for the fiducial case. We show the dust-to-gas ratios for the total (\mathcal{D} ; solid line), the small grains (\mathcal{D}_s ; dotted line), and the large grains (\mathcal{D}_1 ; dashed line).

The evolutionary behaviours of the small and large grain components match the full treatment of grain size distribution in A13 (see their fig. 6). For the case of $\tau_{\text{SF}} = 5$ Gyr in A13, the dust grains are predominantly large at the early stage of galaxy evolution, while small grains are supplied after ~ 1 Gyr when the metallicity reaches $\sim 0.2 Z_{\odot}$. This metallicity level just matches the one at which the rapid increase of the small grain abundance is seen in Fig. 1. The large-grain abundance also increases as a result of coagulation.

3.2 Parameter dependence

The effects of individual processes can be investigated by changing the parameters listed in Table 2. In what follows, we describe each process, where we only change the parameter that regulates it, with the other parameters fixed at the fiducial values.

3.2.1 Dust formation in stellar ejecta

The amount of dust ejected by stars into the ISM is regulated by the condensation efficiency f_{in} in our model, in which we consider the range $f_{\text{in}} = 0.01$ – 0.1 . In Fig. 2, we show the relation between dust-to-gas ratio and metallicity for $f_{\text{in}} = 0.1, 0.03,$ and 0.01 . We also present the small-to-large grain abundance ratio, $\mathcal{D}_s/\mathcal{D}_1$. We observe that the difference in f_{in} leads to a different dust-to-gas ratio proportional to f_{in} at low metallicity before accretion drastically increases the dust-to-gas ratio. The metallicity at which accretion becomes efficient (critical metallicity; Section 4.3) is insensitive to f_{in} . After this rapid increase, all the lines converge into the same \mathcal{D} – Z relation, since the stellar dust production has little influence on the total dust mass compared with accretion at high metallicity.

As shown in Fig. 2, the small-to-large grain abundance ratio, $\mathcal{D}_s/\mathcal{D}_1$, is smaller for a smaller value of f_{in} at low metallicity, simply because the small grain production by shattering is less efficient for small f_{in} (i.e. small large-grain abundance). Associated with the rapid increase of \mathcal{D} by accretion, there appears an epoch at which $\mathcal{D}_s/\mathcal{D}_1$ reaches its peak. At this stage, $\mathcal{D}_s/\mathcal{D}_1$ reaches a larger value for smaller f_{in} simply because the increase of \mathcal{D}_s is prominent if we normalize it to \mathcal{D}_1 , which is smaller at this stage for smaller f_{in} . After this rapid increase, the small-to-large grain abundance ratio converges to a constant value ~ 0.1 , which is independent of

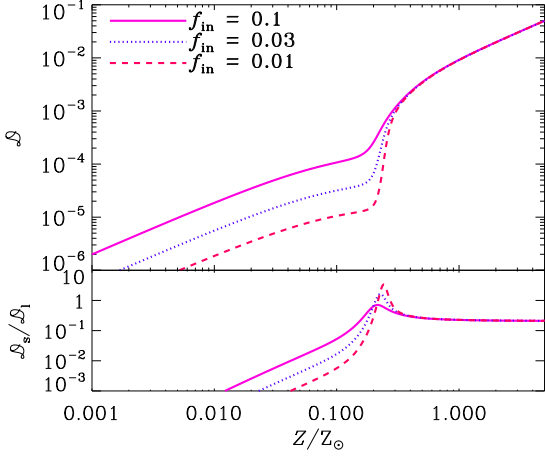


Figure 2. Same as Fig. 1 but for various dust condensation efficiencies in stellar ejecta f_{in} . In the upper window, the total dust-to-gas ratio \mathcal{D} is shown. The solid, dotted, and dashed lines show the cases with $f_{\text{in}} = 0.1$, 0.03, and 0.01, respectively. In the lower window, the small-to-large grain abundance ratio is shown.

f_{in} ; this value is determined by the balance between shattering and coagulation (Section 4.2).

3.2.2 Dust destruction in SN shocks

We examine the effect of dust destruction in SN shocks, i.e. the dependence on β_{SN} . In Fig. 3, we show the relation between dust-to-gas ratio and metallicity for $\beta_{\text{SN}} = 9.65$, 19.3, and 4.83 (i.e. the fiducial case, two times stronger destruction, and two times weaker destruction). The difference in β_{SN} starts to appear around $Z \sim 0.05 Z_{\odot}$, after which the increase of \mathcal{D} is more suppressed for a larger destruction efficiency. This metallicity level is roughly estimated by $Z_{\text{dest}} = \mathcal{V}_Z / \beta_{\text{SN}} \sim 0.067 (\mathcal{V}_Z / 0.013) (\beta_{\text{SN}} / 9.65)^{-1} Z_{\odot}$ (Section 4.1; Kuo et al. 2013), and is marked in Fig. 3 for $\beta_{\text{SN}} = 9.65$ (and $\mathcal{V}_Z = 0.013$, which is unchanged throughout this paper).

Just after the slight suppression of dust mass increase around Z_{dest} , the dust-to-gas ratio (especially, the small-grain dust-to-gas ratio) rapidly increases because of the dust mass growth by the accretion on the small grains created by shattering. This occurs at the critical metallicity of accretion. Above this critical metallicity, the dust growth time-scale becomes shorter than the destruction time-scale so that accretion overcomes the dust destruction effect. The dust-to-gas ratio after the rapid growth is also smaller for larger β_{SN} since the dust abundance (more precisely, the dust-to-metal ratio) is determined by the balance between accretion and destruction at high metallicity (Section 4.2). The small-to-large grain abundance ratio, on the other hand, is determined by the balance between shattering and coagulation at high metallicity (Section 4.2) so that it is insensitive to β_{SN} at $Z \gtrsim 0.7 Z_{\odot}$. Note that, although dust destruction and accretion indeed have a consequence on the relative abundance of small and large grains, the dominant mechanism is shattering and coagulation, which, however, do not change the total dust mass.

We also examine the case of $\alpha < 1$, which corresponds to enhanced destruction of small grains compared with large grains. In Fig. 3, we observe that the small value of α delays the dust mass growth by accretion. This is because accretion is suppressed be-

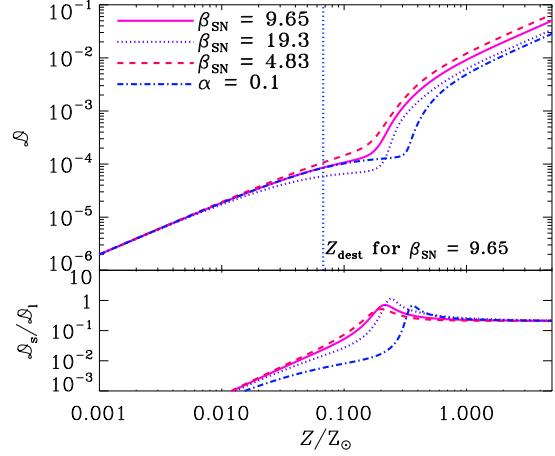


Figure 3. Same as Fig. 2 but for various destruction efficiencies parameterized by β_{SN} and α . The solid, dotted, and dashed curves show the results with $\beta_{\text{SN}} = 9.65$, 19.3, and 4.83, respectively ($\alpha = 1$). The dot-dashed curve represents the case with $\alpha = 0.1$ (enhanced destruction of small grains) for $\beta_{\text{SN}} = 9.65$. The vertical dotted line marks the characteristic metallicity Z_{dest} at which the dust loss by destruction becomes comparable to the dust supply from stars for $\beta_{\text{SN}} = 9.65$.

cause more small grains are destroyed. Nevertheless, because of the strong metallicity dependence of accretion, accretion still becomes efficient enough around $Z = 0.3 Z_{\odot}$ to boost $\mathcal{D}_s / \mathcal{D}_l$ and \mathcal{D} .

3.2.3 Accretion

As explained in Section 2.3, we vary τ_{cl} to change the efficiency of accretion. In Fig. 4, we show the relation between dust-to-gas ratio and metallicity for various τ_{cl} . As expected, the rapid increase of \mathcal{D} by accretion occurs earlier for longer τ_{cl} (i.e. more efficient accretion). As assumed in this model based on Hirashita (2012) (see also Section 2.1), accretion increases the abundance of the small grains. Therefore, the rapid rise of \mathcal{D} is associated with the increase of $\mathcal{D}_s / \mathcal{D}_l$. After this rapid growth is settled, the \mathcal{D} - Z and $\mathcal{D}_s / \mathcal{D}_l$ - Z relations converge to the curves independent of τ_{cl} at high metallicity. In fact, at high metallicity, grain growth by accretion is saturated, and $\mathcal{B} \simeq (Z - \mathcal{D}) / \mathcal{D}_s$ (equation 10; this means that all the gas phase metals are accreted onto the small grains in dense clouds), which is independent of τ_{cl} .

3.2.4 Shattering

We also change the shattering time-scale, which is scaled with the value $\tau_{\text{sh},0}$ at the Milky Way dust-to-gas ratio. From Fig. 5, we observe that the small-to-large grain abundance ratio is largely affected by the shattering time-scale. This ratio is roughly proportional to $\tau_{\text{sh},0}$ except at the epoch when accretion rapidly raise the small-grain abundance. Furthermore, the metallicity at which the accretion increase the dust-to-gas ratio is smaller for a shorter shattering time-scale. However, once accretion starts to increase the dust mass, it rapidly boosts the small-to-large grain abundance ratio, so that the resulting track on the \mathcal{D} - Z plane is not very sensitive to shattering. Shattering does not directly change the dust abundance, but it plays an important role in the total dust abundance through its capability of producing a large number of small

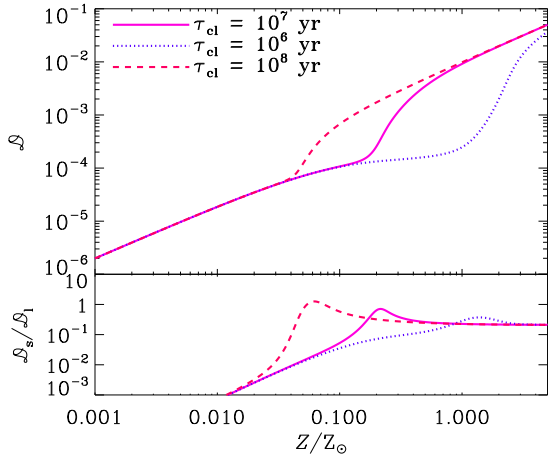


Figure 4. Same as Fig. 2 but for various dense cloud lifetimes (τ_{cl}), which regulate the efficiency of accretion. The solid, dotted, and dashed lines show the results with $\tau_{\text{cl}} = 10^7$, 10^6 , and 10^8 yr, respectively.

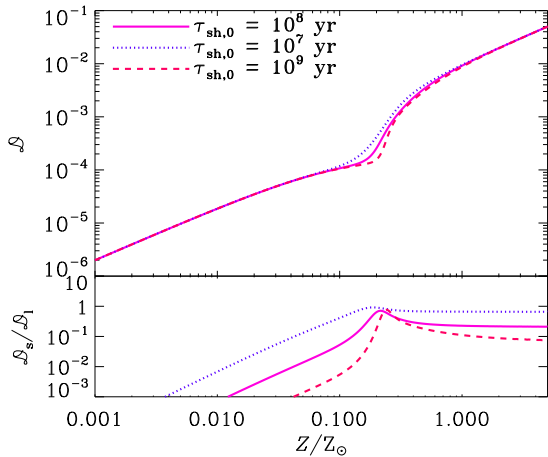


Figure 5. Same as Fig. 2 but for various shattering time-scales at the Milky Way dust-to-gas ratio ($\tau_{\text{sh},0}$). The solid, dotted, and dashed lines show the results with $\tau_{\text{sh},0} = 10^8$, 10^7 , and 10^9 yr, respectively.

grains, whose growth by accretion is of fundamental importance in the dust mass increase (see also Kuo & Hirashita 2012 and A13).

3.2.5 Coagulation

For the variation of the coagulation time-scale, we show the results in Fig. 6. We observe that the small-to-large grain abundance ratio is independent of $\tau_{\text{co},0}$ at low metallicity ($Z < 0.03 Z_{\odot}$) while it is larger for larger $\tau_{\text{co},0}$. This is because coagulation has little influence on the dust evolution at low metallicity and the small grains are efficiently converted into large grains after the dust-to-gas ratio has become large enough for coagulation to occur. The metallicity at which accretion rapidly increases the dust-to-gas ratio is not sensitive to the coagulation time-scale, although the growth is significantly suppressed for the case of the shortest $\tau_{\text{co},0}$, since a major part of the small grains are converted into the large grains before they accrete the gas-phase metals. The final dust-to-gas ratio at high metallicity is insensitive to the coagulation time-scale.

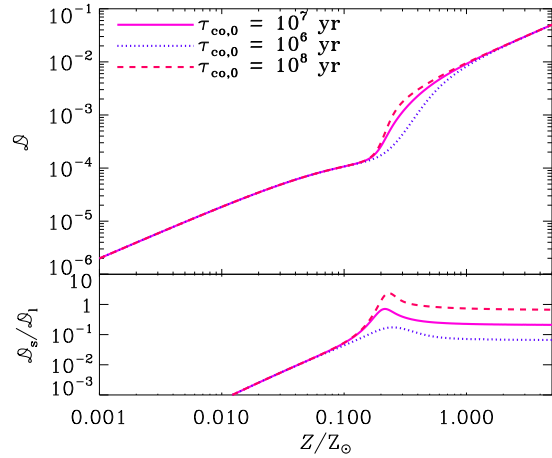


Figure 6. Same as Fig. 2 but for various coagulation time-scales. The solid, dotted, and dashed lines show the results with $\tau_{\text{co},0} = 10^7$, 10^6 , and 10^8 yr, respectively.

3.2.6 Star formation time-scale

We also change the star formation time-scale, τ_{SF} , which governs the metal-enrichment time-scale of the galaxy. This time-scale affects shattering and coagulation, since β_{sh} (β_{co}) is determined by the ratio of τ_{SF} to τ_{sh} (τ_{co}). In Fig. 7, we show the results for $\tau_{\text{SF}} = 5 \times 10^8$, 5×10^9 , and 5×10^{10} yr. The D - Z relation is hardly affected by τ_{SF} . In contrast, Inoue (2003) concluded that D - Z is largely affected by τ_{SF} . This is because Inoue (2003) moved τ_{SF} freely, while we assume the proportionality between τ_{SF} and τ_{acc} through equations (9) and (12) since both star formation and accretion occur in the dense ISM.

As observed in the bottom panel of Fig. 7, the small-to-large grain abundance ratio is largely varied by the change of τ_{SF} especially at low metallicity. At low metallicity, the small-grain abundance is governed not only by the abundance of the large grains, from which the small grains are produced by shattering, but also by how much shattering can occur in the metal-enrichment time-scale (i.e., $\tau_{\text{SF}}/\tau_{\text{sh},0}$). Therefore, if we take the small-to-large grain abundance ratio, the factor $\tau_{\text{SF}}/\tau_{\text{sh},0}$ remains (see equation 22 for more quantification). Thus, D_s/D_1 is larger for longer τ_{SF} at low metallicity. The ‘overshoot’ of D_s/D_1 around $0.2 Z_{\odot}$ does not appear for the longest τ_{SF} , since the equilibrium between shattering and coagulation is achieved before the metallicity reaches that value. Indeed, Fig. 7 shows that D_s/D_1 converges to a constant value determined by the equilibrium between shattering and coagulation (see Section 4.2) even before accretion rapidly raise the dust-to-gas ratio for the longest τ_{SF} . The ‘overshoot’ is the most prominent for the shortest τ_{SF} . All the three cases finally converge to the same values of D_s/D_1 determined by the equilibrium between shattering and coagulation.

3.3 Monte Carlo plots

To summarize the variation of the D - Z and D_s/D_1 - Z relations, we perform a Monte Carlo simulation, varying the parameters within the ranges examined above (Table 2). Such a Monte Carlo approach to predict the variation of the evolutionary tracks in the relation between dust-to-gas ratio and metallicity has already been performed by Mattsson et al. (2014). We apply their method to our formula-

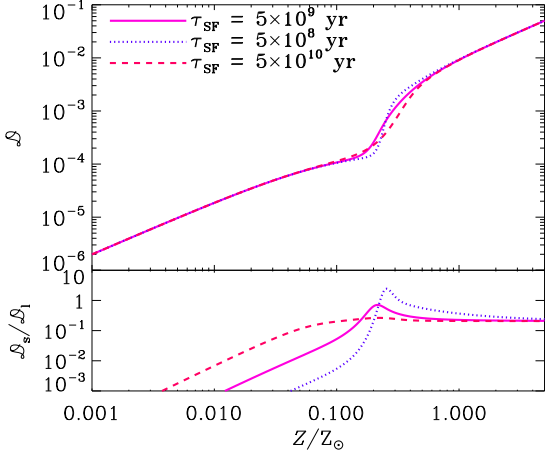


Figure 7. Same as Fig. 2 but for various star formation time-scales. The solid, dotted, and dashed lines show the results with $\tau_{\text{SF}} = 5 \times 10^9$, 5×10^8 , and 5×10^{10} yr, respectively.

tion and set of parameters. For simplicity, we assume a uniform distribution for the logarithm of each parameter in the range shown in Table 2. For each set of parameter values chosen, we calculate the evolutionary track on the \mathcal{D} - Z and $\mathcal{D}_s/\mathcal{D}_1$ - Z plane. By repeating this for 100,000 random choices of the parameter set, we obtain the density distribution of evolutionary tracks. This implicitly assume that the metallicity distribution is uniform. In other words, the slice at each metallicity gives the probabilities of \mathcal{D} and $\mathcal{D}_s/\mathcal{D}_1$ at the metallicity, $P_1(\mathcal{D}|Z) d \log \mathcal{D}$ and $P_2(\mathcal{D}_s/\mathcal{D}_1|Z) d(\mathcal{D}_s/\mathcal{D}_1)$, respectively.

In Fig. 8, we show the colour maps of $P_1(\mathcal{D}|Z)$ and $P_2(\mathcal{D}_s/\mathcal{D}_1|Z)$. For the \mathcal{D} - Z relation, P_1 is almost constant at low metallicity simply because we assume uniform distribution for $\log f_{\text{in}}$, which is the only factor affecting the \mathcal{D} - Z relation. At $Z \gtrsim 0.1 Z_{\odot}$, accretion becomes the dominant mechanism of dust mass increase, producing the peak of P_1 at large dust-to-gas ratio. At $0.1 \lesssim Z/Z_{\odot} \lesssim 1$, the distribution of dust-to-gas ratio is bimodal with different dust production mechanisms: the upper/lower peak is composed of the objects in which accretion/stellar ejecta is the main dust production mechanism. Since the dust mass increase by accretion occurs rapidly, these two branches separate clearly, producing the bimodality.

The distribution of small-to-large grain abundance ratio in Fig. 8 (bottom panel) shows a large dispersion at low metallicity, reflecting the variations of f_{in} (Fig. 2) and $\tau_{\text{sh},0}/\tau_{\text{SF}}$ (Figs. 5 and 7) (see also Section 4.1). The overshoot of the small-to-large grain abundance ratio is clearly seen around $Z \sim 0.2 Z_{\odot}$. At high metallicity the small-to-large grain abundance ratio converges to the values determined by the shattering and coagulation time-scales (Section 4.2); thus, the dispersion of $\mathcal{D}_s/\mathcal{D}_1$ at high metallicity reflects the dispersions of $\tau_{\text{sh},0}$ and $\tau_{\text{co},0}$.

For reference, we also plot the observational data of nearby galaxies in Fig. 8. The data are taken from Rémy-Ruyer et al. (2014) (see also Rémy-Ruyer et al. 2013). They combined three different samples: the Dwarf Galaxy Survey (Madden et al. 2013), the KINGFISH survey (Kennicutt et al. 2011) and a subsample of Galametz et al. (2011). They derived the dust masses by fitting the SED with the model presented in Galliano et al. (2011), and took the atomic and molecular masses in the literature. For the CO-to- H_2 conversion factor, we adopt their metallicity-dependent case,

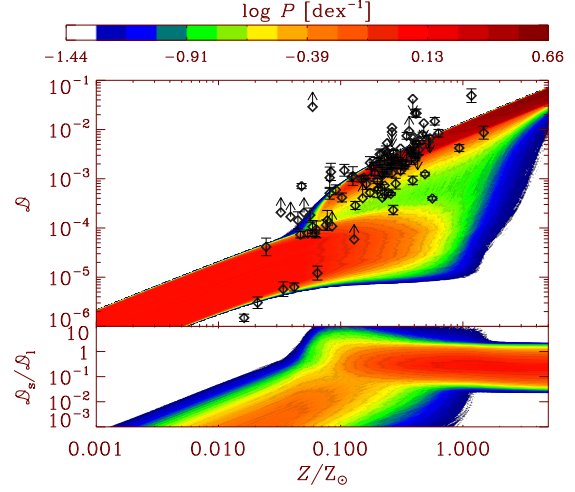


Figure 8. Probability distribution on the \mathcal{D} - Z and $\mathcal{D}_s/\mathcal{D}_1$ - Z planes for the Monte Carlo simulation with randomly selected values of the parameters. The probability P ($= P_1$ in the upper panel and P_2 in the lower panel) at each metallicity is shown with the color maps. The scale is shown in the colour bar above the figures. For reference, we also plot the observational data of nearby galaxies taken from Rémy-Ruyer et al. (2014) (diamonds with error bars). The arrows show the upper or lower limits depending on the direction.

but the results and discussions does not change even if we adopt the Milky Way conversion factor. For the solar metallicity, we adopt $12 + \log(\text{O}/\text{H}) = 8.93$ (Anders & Grevesse 1989) to be consistent with the normalization used for the models.

In Fig. 8, we observe that the distribution of the data is broadly consistent with the colour map. The trend from the low dust-to-gas ratio at low metallicity to the high dust-to-gas ratio at high metallicity is correctly reproduced. In particular, the region with the highest probabilities on the \mathcal{D} - Z diagram at $0.1 \lesssim Z/Z_{\odot} \lesssim 1$, where the main dust formation mechanism is accretion, matches the concentration of the observational data. This supports the necessity of accretion for this metallicity range (see also the models in Rémy-Ruyer et al. 2014 and Zhukovska (2014), and figure 5 in de Bressan et al. 2014 for comparisons with the same data). A few low- \mathcal{D} objects in this metallicity range are consistent with the lower branch (secondary peak) of P_1 in which the dust is predominantly supplied from stars. At lower metallicities, the stellar dust production explains the data well, although the number of low-metallicity objects is still small. Considering the simplicity of our models, we judge that the model and the choice of the parameter ranges are successful.

4 DISCUSSION

We analyze the behaviours of \mathcal{D} and $\mathcal{D}_s/\mathcal{D}_1$ at various metallicities.

4.1 Evolution at low metallicity

At low metallicity, if we keep the terms up to the first order for Z in equation (17), we obtain for the large grains

$$\mathcal{Y}_Z \frac{d\mathcal{D}_1}{dZ} \simeq f_{\text{in}}(\mathcal{R}Z + \mathcal{Y}_Z) - (\beta_{\text{SN}} + \mathcal{R})\mathcal{D}_1. \quad (20)$$

The zeroth order indicates the solution $\mathcal{D}_1 \simeq f_{\text{in}}Z$. This means that only the stellar dust contributes to the dust enrichment at

low metallicity. If we put this solution on the right hand side in equation (20), we obtain $d\mathcal{D}_1/dZ \simeq f_{\text{in}} - \beta_{\text{SN}}f_{\text{in}}Z/\mathcal{Y}_Z$, where the second term indicates the destruction in SN shocks. Comparing the first and second terms on the right-hand side of this equation, we find that the dust destruction almost cancels the dust formation by stars at a characteristic metallicity, Z_{dest} : $Z \sim Z_{\text{dest}} \equiv \mathcal{Y}_Z/\beta_{\text{SN}} \sim 0.067(\mathcal{Y}_Z/0.013)(\beta_{\text{SN}}/9.65)^{-1} Z_{\odot}$, the corresponding dust-to-gas ratio being $\mathcal{D}_1 \sim f_{\text{in}}Z_{\text{dest}} \sim 1.3 \times 10^{-4}(\mathcal{Y}_Z/0.013)(\beta_{\text{SN}}/9.65)^{-1}(f_{\text{in}}/0.1)$. Indeed, $Z = Z_{\text{dest}}$, marked in Fig. 3, roughly corresponds to the metallicity level at which the increase of dust-to-gas ratio slows down significantly.

For the small grains, if we only take the lowest order for Z , the second-order term representing shattering remains:

$$\mathcal{Y}_Z \frac{d\mathcal{D}_s}{dZ} = \beta_{\text{sh}}\mathcal{D}_1 = \frac{\tau_{\text{SF}}}{\tau_{\text{sh},0}} \frac{1}{\mathcal{D}_{\text{MW},s}} (f_{\text{in}}Z)^2, \quad (21)$$

where we used the solution at low metallicity, $\mathcal{D}_1 = f_{\text{in}}Z$. Solving this, and using the low-metallicity solution for \mathcal{D}_1 , we obtain the expression valid for low metallicities:

$$\begin{aligned} \frac{\mathcal{D}_s}{\mathcal{D}_1} &\simeq \frac{f_{\text{in}}Z^2}{3\mathcal{Y}_Z\mathcal{D}_{\text{MW},1}} \left(\frac{\tau_{\text{SF}}}{\tau_{\text{sh},0}} \right) \\ &= 0.073 \left(\frac{f_{\text{in}}}{0.1} \right) \left(\frac{\tau_{\text{SF}}}{5 \times 10^9 \text{ yr}} \right) \left(\frac{\tau_{\text{sh},0}}{10^8 \text{ yr}} \right)^{-1} \\ &\quad \times \left(\frac{Z}{0.1 Z_{\odot}} \right)^2, \end{aligned} \quad (22)$$

where we fix $\mathcal{Y}_Z = 0.013$ and $\mathcal{D}_{\text{MW},1} = 0.007$. This nicely explains the behaviour and parameter dependence of the small-to-large grain abundance ratio at low metallicity (note especially the dependence on f_{in} , $\tau_{\text{sh},0}$, and τ_{SF} shown in Figs. 2, 5, and 7, respectively).

4.2 Evolution at high metallicity

At high metallicity, the dust-to-gas ratio increases in proportion to the metallicity, which means that the dust-to-metal ratio \mathcal{D}/Z converges to a constant value. We also observe that the small-to-large grain abundance ratio converges to a constant value at high metallicity. These characteristics are analyzed by taking the differentials of \mathcal{D}_s/Z and \mathcal{D}_1/Z as follows.

At high metallicity, we can neglect the dust supply from stars, and the dust content is determined by interstellar processing (accretion, destruction, shattering and coagulation). By keeping those terms, the differentials of \mathcal{D}_s/Z and \mathcal{D}_1/Z are expressed, using equations (17) and (18) as

$$\mathcal{Y}_Z \frac{d}{dZ} \left(\frac{\mathcal{D}_1}{Z} \right) \simeq \frac{1}{Z} [\beta_{\text{co}}\mathcal{D}_s - (\beta_{\text{SN}} + \beta_{\text{sh}})\mathcal{D}_1], \quad (23)$$

$$\mathcal{Y}_Z \frac{d}{dZ} \left(\frac{\mathcal{D}_s}{Z} \right) \simeq \frac{1}{Z} \left[\beta_{\text{sh}}\mathcal{D}_1 - \left(\frac{\beta_{\text{SN}}}{\alpha} + \beta_{\text{co}} - \beta_{\text{acc}} \right) \mathcal{D}_s \right]. \quad (24)$$

The terms with β_{co} and β_{sh} grow as metallicity (or dust-to-gas ratio) increases; thus, they eventually become dominant. This indicates that coagulation and shattering balance at high metallicity. In other words, $\beta_{\text{co}}\mathcal{D}_s - \beta_{\text{sh}}\mathcal{D}_1 \simeq 0$, leading to the expectation that the small-to-large grain abundance ratio converge to $\mathcal{D}_s/\mathcal{D}_1 \simeq \beta_{\text{sh}}/\beta_{\text{co}} = \tau_{\text{co}}/\tau_{\text{sh}}$. Using equations (7) and (8), we obtain

$$\frac{\mathcal{D}_s}{\mathcal{D}_1} \simeq \left(\frac{\mathcal{D}_{\text{MW},s} \tau_{\text{co},0}}{\mathcal{D}_{\text{MW},1} \tau_{\text{sh},0}} \right)^{1/2} \quad (25)$$

for the high-metallicity regime. If we put the fiducial values, we obtain $\mathcal{D}_s/\mathcal{D}_1 \simeq 0.21$, explaining the value at high metallicity very well. Equation (25) also gives correct estimates for other values of $\tau_{\text{sh},0}$ and $\tau_{\text{co},0}$.

If we add equations (23) and (24), we obtain the equation for the total dust-to-metal ratio:

$$\mathcal{Y}_Z \frac{d}{dZ} \left(\frac{\mathcal{D}}{Z} \right) \simeq \frac{1}{Z} [-\beta_{\text{SN}}\delta\mathcal{D} + \beta_{\text{acc}}\mathcal{D}_s], \quad (26)$$

where

$$\delta \equiv 1 + \left(\frac{1}{\alpha} - 1 \right) \frac{\mathcal{D}_s}{\mathcal{D}}. \quad (27)$$

If $\alpha = 1$, $\delta = 1$. For high metallicity, $\beta_{\text{acc}} = \beta/\epsilon \sim (Z - \mathcal{D})/(\epsilon\mathcal{D}_s)$ ($y \rightarrow \infty$, which corresponds to the most efficient accretion, in equation 10), so that we obtain

$$\frac{\mathcal{D}}{Z} \simeq \frac{1}{\epsilon\beta_{\text{SN}}\delta + 1}. \quad (28)$$

For $\alpha = 1$ ($\delta = 1$), this gives the same result as Hirashita & Kuo (2011). For the fiducial case, $\mathcal{D}/Z \sim 0.5$, which explains the dust-to-metal ratio at high metallicity. This is consistent with the metal depletion in the Milky Way (e.g. Kimura, Mann, & Jessberger 2003). If the small grains are more easily destroyed (i.e. $\alpha < 1$, so $\delta > 1$), the dust-to-metal ratio is suppressed, which reflects the fact that accretion is also suppressed because of the destruction of the small grains. This explains the suppression of \mathcal{D} in the case of $\alpha = 0.1$ compared with the other cases in Fig. 3.

4.3 Critical metallicity for accretion

The most remarkable increase of dust-to-gas ratio is induced by accretion. Because of its metallicity dependence, accretion occurs after the ISM is enriched with metals. The metallicity level at which accretion starts to increase the dust-to-gas ratio significantly is referred to as the critical metallicity for accretion (Inoue 2011; Asano et al. 2013b). Following Hirashita & Kuo (2011), we estimate the critical metallicity with $\beta_{\text{SN}}\mathcal{D} = \beta_{\text{acc}}\mathcal{D}_s$, which means that accretion starts to increase the dust-to-gas ratio more than SN destruction decreases it (equation 19; note that $\mathcal{R} \ll \beta_{\text{SN}}$ and that $\beta'_{\text{SN}} = \beta_{\text{SN}}$ for $\alpha = 1$). We observe from Figs. 2–6 that $\mathcal{D}_s/\mathcal{D}_1$ approaches ~ 1 except for the case of strong coagulation (i.e. $\tau_{\text{co},0} \lesssim 10^6$ yr). Thus, we adopt $\mathcal{D}_s \simeq \mathcal{D}/2$, obtaining $\beta_{\text{acc}}/2 \simeq \beta_{\text{SN}}$ at the critical metallicity.

In Fig. 9, we compare $\beta_{\text{acc}}/2$ and β_{SN} for the fiducial case. As the metallicity increases, β_{acc} grows. The metallicity at the crossover of β_{SN} and $\beta_{\text{acc}}/2$ is the critical metallicity, which is $0.12 Z_{\odot}$ in this case. Around this metallicity, the rapid increase of dust-to-gas ratio indeed occurs in Fig. 1.

In Fig. 9, we also show β_{sh} and β_{co} , which are proportional to \mathcal{D}_1 and \mathcal{D}_s , respectively. We observe that β_{co} becomes comparable to β_{acc} just above the critical metallicity because the rapid increase of the small grain abundance by accretion enhances the coagulation rate. The metallicity at the maximum of $\mathcal{D}_s/\mathcal{D}_1$ roughly corresponds to the point where $\beta_{\text{co}} \simeq \beta_{\text{acc}}$. After that, coagulation becomes efficient and convert the small grains into the large grains. Thus, it is predicted that at medium metallicity galaxies experience an epoch at which the abundance of small grains is enhanced.

It is possible to make a rough estimate of the maximum $\mathcal{D}_s/\mathcal{D}_1$. As discussed above, $\beta_{\text{co}} \sim \beta_{\text{acc}}$ is satisfied when $\mathcal{D}_s/\mathcal{D}_1$ reaches its maximum. As shown in Fig. 9, β_{acc} saturates above β_{SN} . Thus, we roughly adopt $\beta_{\text{acc}} \sim 3\beta_{\text{SN}}$ for analytic simplicity. Using the definition $\beta_{\text{co}} = \tau_{\text{SF}}/\tau_{\text{co}}$ and equation (7), we ob-

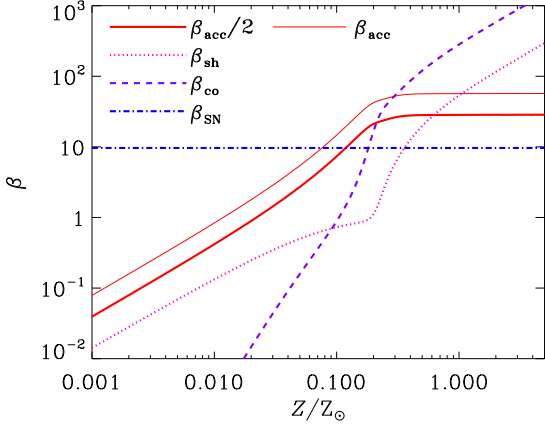


Figure 9. For comparison among the efficiencies of various processes, we plot $\beta_{\text{acc}}/2$, β_{acc} , β_{sh} , β_{co} , and β_{SN} as a function of metallicity (thick solid, thin solid, dotted, dashed, and dot-dashed lines, respectively) for the fiducial case.

tain $\mathcal{D}_s \sim 3\beta_{\text{SN}}(\tau_{\text{co},0}/\tau_{\text{SF}})\mathcal{D}_{\text{MW},s}$. For the large grains, just before the rapid increase by coagulation, \mathcal{D}_l is assumed to be determined by the balance between the formation in stellar ejecta and the destruction by SNe, so that $\mathcal{D}_l \sim f_{\text{in}}Z_{\text{dest}} \sim 1.3 \times 10^{-4}(\mathcal{Y}_Z/0.013)(\beta_{\text{SN}}/9.65)^{-1}(f_{\text{in}}/0.1)$ (Section 4.1). Thus, the maximum $\mathcal{D}_s/\mathcal{D}_l$ is estimated as

$$\begin{aligned} \left(\frac{\mathcal{D}_s}{\mathcal{D}_l}\right)_{\text{max}} &\sim \left(\frac{3\beta_{\text{SN}}\mathcal{D}_{\text{MW},s}}{f_{\text{in}}Z_{\text{dest}}}\right) \left(\frac{\tau_{\text{co},0}}{\tau_{\text{SF}}}\right) \\ &\sim 1.3 \left(\frac{\beta_{\text{SN}}}{9.65}\right)^2 \left(\frac{\tau_{\text{co},0}}{10^7 \text{ yr}}\right) \left(\frac{\tau_{\text{SF}}}{5 \times 10^9 \text{ yr}}\right)^{-1} \\ &\quad \times \left(\frac{f_{\text{in}}}{0.1}\right)^{-1} \left(\frac{\mathcal{Y}_Z}{0.013}\right)^{-1} \left(\frac{\mathcal{D}_{\text{MW},s}}{0.003}\right). \end{aligned} \quad (29)$$

This roughly explains the value of the maximum small-to-large grain abundance ratio and its dependence on f_{in} , β_{SN} , $\tau_{\text{co},0}$, and τ_{SF} shown in Figs. 2, 3, 6, and 7, respectively. We also find in the above expression that the maximum $\mathcal{D}_s/\mathcal{D}_l$ is independent of shattering, which is consistent with the constant maximum $\mathcal{D}_s/\mathcal{D}_l$ achieved in Fig. 5.

4.4 Evolution of grain size distribution

Our simple two-size approach successfully catches the characteristics of grain size evolution in A13’s full calculation of grain size distribution. In the early stage of galaxy evolution when the metallicity is much smaller than the critical metallicity of accretion, the dust is predominantly enriched by stellar ejecta. In this stage, the large grains dominate the dust content. The only path of small grain formation is shattering, which becomes more and more efficient as the system is enriched with the large grains. At a metallicity level referred to as the critical metallicity, the abundance of small grains formed by shattering becomes large enough to activate the grain growth by accretion, which contributes to the rapid increase of dust-to-gas ratio. Associated with this phase, the small-to-large grain abundance ratio becomes the largest in the entire life of the galaxy. After the increase of dust-to-gas ratio by accretion is saturated, the small-to-large grain abundance ratio is governed by the balance between shattering and coagulation.

Equation (25), valid for high-metallicity galaxies, can be

used to constrain the ratio of the coagulation time-scale to the shattering time-scale. In particular, in the Milky Way, the self-consistent small-to-large grain abundance ratio can be estimated as $\mathcal{D}_{\text{MW},s}/\mathcal{D}_{\text{MW},l} \simeq \tau_{\text{co},0}/\tau_{\text{sh},0}$. Using $\mathcal{D}_{\text{MW},s}/\mathcal{D}_{\text{MW},l}$ estimated in Section 2.2 based on the MRN grain size distribution, we obtain $\tau_{\text{co},0}/\tau_{\text{sh},0} \simeq 0.43$ in the Milky Way. The ratio should depend on the mass fractions of various ISM phases (Seok et al. 2014). Although it is difficult to determine the absolute values of $\tau_{\text{sh},0}$ and $\tau_{\text{co},0}$, putting a constraint on the ratio of these two time-scales is a big step to understand the evolution of grain size distribution in galaxies.

5 FUTURE PROSPECTS

5.1 Implementation in complex galaxy evolution models

As mentioned in the Introduction, one of the major purposes of developing computationally light models for the evolution of grain size distribution is to implement it in complex galaxy evolution models. It is extremely difficult to calculate the full evolution of grain size distribution, since it is simply expected that the computational time increases in proportion to the number of grain size bins. Many galaxy evolution models already treat metal enrichment so that it is rather straightforward to calculate equations (17) and (18) in such models. We could apply them to each galaxy or each SPH particle. Variation of $\tau_{\text{co},0}$ and $\tau_{\text{sh},0}$ can also be included based on the mixture of various ISM phases (Seok et al. 2014) or based on the density and temperature of each SPH particle (Hirashita & Yan 2009), as straightforward extensions.

As a trade-off of the simplicity, there is of course a demerit of using such a simple model as developed in this paper. Since it does not treat the full information of the grain size distribution, we need to assume a functional form of grain size distribution in calculating observational dust properties. Representative observational quantities related to dust are extinction curves and infrared dust emission SEDs. In the following subsections, we discuss how to calculate these quantities using the two-size model, in order to provide future prospects. The real implementation of our models to galaxy evolution models will be done in future work.

Here we propose to use a ‘modified-lognormal function’ for the grain size distributions of the small and large grains (the grain size distribution is defined so that $n_i(a) da$ is the number of grains per hydrogen nucleus in the range of grain radii between a and $a + da$):

$$n_i(a) = \frac{C_i}{a^4} \exp \left\{ -\frac{[\ln(a/a_{0,i})]^2}{2\sigma^2} \right\}, \quad (30)$$

where subscript i indicates the small ($i = s$) or large ($i = l$) grain component, C_i is the normalization constant, and $a_{0,i}$ and σ are the central grain radius and the standard deviation of the lognormal distribution, respectively. The functional form is adopted so that the mass distribution $\propto a^3 n_i(a)$ is lognormal. We adopt $a_{0,s} = 0.005 \mu\text{m}$, $a_{0,l} = 0.1 \mu\text{m}$, and $\sigma = 0.75$, to roughly cover the small and large grain size ranges. We hereafter refer to this grain size distribution as the lognormal model. The normalizing constants are determined by

$$\mu m_{\text{H}} \mathcal{D}_i = \int_0^\infty \frac{4}{3} \pi a^3 s n_i(a) da, \quad (31)$$

where $\mu = 1.4$ is the gas mass per hydrogen nucleus, m_{H} is the hydrogen atom mass, and s is the material density of a dust grain.

Therefore, the evolutions of \mathcal{D}_s and \mathcal{D}_l are reduced to those of C_s and C_l , respectively.

5.2 Extinction curves

The extinction at wavelength λ in units of magnitude (A_λ) normalized to the column density of hydrogen nuclei (N_H) is written as

$$\frac{A_\lambda}{N_H} = 2.5 \log e \sum_i \int_0^\infty n_i(a) \pi a^2 Q_{\text{ext}}(a, \lambda), \quad (32)$$

where $Q_{\text{ext}}(a, \lambda)$ is the extinction efficiency factor, which is evaluated by using the Mie theory (Bohren & Huffman 1983) and the same optical constants for silicate and carbonaceous dust in Weingartner & Draine (2001). For simplicity, the mass fractions of silicate and carbonaceous dust are assumed to be 0.54 and 0.46, respectively (Hirashita & Yan 2009). We adopt $s = 3.5$ and 2.24 g cm^{-3} for silicate and carbonaceous dust, respectively (Weingartner & Draine 2001).

In Appendix A, in order to examine how well the lognormal model is capable of approximating the MRN model ($n_i(a) \propto a^{-3.5}$ with $0.001 \mu\text{m} \leq a \leq 0.25 \mu\text{m}$), which is known to reproduce the Milky Way extinction curve well, we compare the extinction curves predicted by these two models under the same small-to-large grain abundance ratio. We confirm that the lognormal model approximately reproduces the Milky Way extinction curve, which means that the lognormal model provides a useful simple approach to predict the extinction curve in the two-size approximation.

Now we examine the extinction curves predicted by our two-size dust evolution models with the fiducial parameter values. In Fig. 10, we show the grain size distributions and the extinction curves at $Z = 0.1, 0.2$, and $1 Z_\odot$. At $Z \lesssim 0.1 Z_\odot$, the extinction curve is flat, reflecting the grain size distribution dominated by the large grains. At this metallicity, the dust content is dominated by the stellar dust production of large grains. At $Z \sim 0.2 Z_\odot$, the small-to-large grain abundance ratio reaches its peak (Fig. 1), and indeed the lognormal model correctly show the enhanced small-grain abundance. At this metallicity, the extinction curve becomes the steepest with the most prominent carbon bump. Afterwards, coagulation pushes the grains to large sizes, and accordingly the extinction curve becomes flatter. The above evolutionary features are in line with the evolution of extinction curves calculated by A13's full treatment of grain size distribution (Asano et al. 2014).

We also examine the variation at solar metallicity based on the dispersion of $\log(\mathcal{D}_s/\mathcal{D}_l)$ calculated by the Monte Carlo method in Section 3.3 (see also Fig. 8). The mean and 1σ variation of $\log(\mathcal{D}_s/\mathcal{D}_l)$ is -0.52 and 0.40 , respectively. The extinction curves corresponding to the 1σ range is shown in Fig. 11. The variation of extinction curves is compared with the variation in the Milky Way. The vertical bars in Fig. 10b show the 1σ range of the Milky Way extinction curves in various lines of sight compiled in Fitzpatrick & Massa (2007) (see also Nozawa & Fukugita 2013). The comparison between the dispersion of the Milky Way extinction curves and that predicted by our models assumes that the dispersion is produced by the scatter of the parameters. These two dispersions are roughly comparable except at the carbon bump where our models predict too large a dispersion. Probably the assumption that the silicate to graphite ratio is constant should be revised in order to reproduce a reasonable scatter of the carbon bump strength, or the optical properties of carbonaceous dust may still need to be revised (Nozawa et al. 2015).

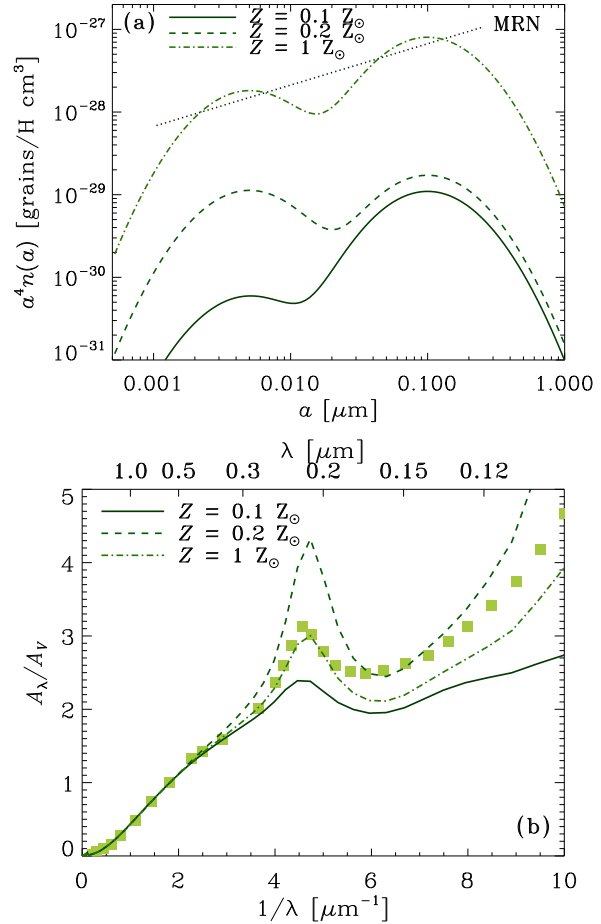


Figure 10. (a) Grain size distributions in the lognormal model for the fiducial model. The solid, dashed, and dot-dashed lines show the size distributions at $Z = 0.1, 0.2$, and $1 Z_\odot$, respectively. The grain size distributions are presented by multiplying a^4 to show the mass distribution per log a . The MRN grain size distribution is shown by the dotted line as a reference. (b) Extinction curves calculated for the grain size distributions in Panel (a). The extinction is normalized to the value at the V band ($0.55 \mu\text{m}$). The solid, dashed, and dot-dashed lines show the extinction curves at $Z = 0.1, 0.2$, and $1 Z_\odot$, respectively. The filled squares show the observed mean extinction curve of the Milky Way taken from Pei (1992).

5.3 Prospect for dust emission SED models

Another important observational feature that reflects the dust properties is the dust emission SED at infrared and submillimetre wavelengths. At long wavelengths ($\gtrsim 100 \mu\text{m}$), the dust responsible for the emission can be treated as being in radiative equilibrium with the ambient interstellar radiation field, so that the SED shape depends mainly on the total dust amount and the equilibrium dust temperature (Désert, Boulanger, & Puget 1990; Li & Draine 2001). Therefore, the evolution of the grain size distribution is not very important at those long wavelengths.

In contrast, at wavelengths $\lesssim 60 \mu\text{m}$, the emission is governed by small grains ($\lesssim 0.01 \mu\text{m}$), whose heat capacities are so small that they are transiently heated by discrete photon inputs (Draine & Anderson 1985). Thus, the spectrum at $\lesssim 60 \mu\text{m}$ is sensitive to the grain size distribution. Moreover, some spectral features specific to certain dust species such as PAH features are prominent at $\lesssim 20 \mu\text{m}$, which means that a detailed spectral model-

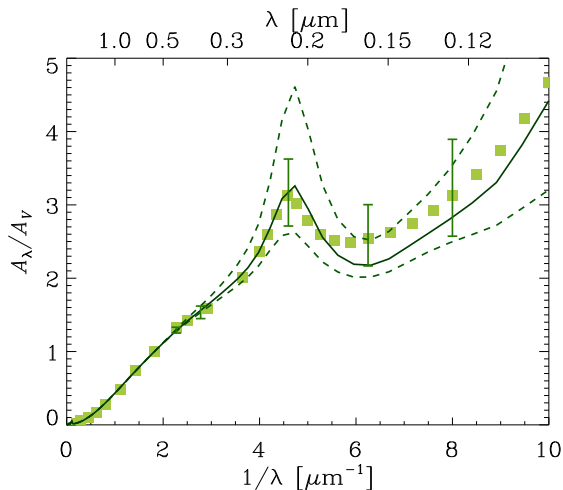


Figure 11. Extinction curves calculated with the lognormal model for the mean (solid line), and the upper and lower ranges expected for the dispersion (dotted lines) in our Monte Carlo simulation. The filled squares are the same data as in Panel (a), and the vertical bars show the 1σ dispersion for the observed Milky Way extinction curves taken from Fitzpatrick & Massa (2007) (see also Nozawa & Fukugita 2013).

ing is necessary for this wavelength range. Therefore, the two-size models developed in this paper would be too rough to predict the evolution of dust SED at such short wavelengths.

Nevertheless, we could prepare spectral templates for the small and large grains, and mix them according to the small-to-large grain abundance ratio calculated by the two-size models. If we separately calculate various grain species, we could also sum up all the templates calculated for various dust species. In this way, we will be able to predict the evolution of dust emission SEDs without consuming much computational time.

6 CONCLUSION

We have examined a possibility of treating the evolution of grain size distribution with two representing grain radii, motivated by the fact that a full treatment of grain size distribution is too heavy to be incorporated in cosmological galaxy evolution models. In this ‘two-size approximation’, we consider small (grain radius $a < 0.03\ \mu\text{m}$) and large ($a > 0.03\ \mu\text{m}$) grains and treat the evolution of the mass fractions of these two components through various processes of grain formation and processing. We include dust supply from stellar ejecta, destruction in SN shocks, dust growth by accretion, grain growth by coagulation and grain disruption by shattering. First we demonstrated that the following features of the full treatment of grain size distribution by A13 are correctly reproduced by the two-size approximation. The dust enrichment starts with the supply of the large grains from stars. The dominant dust production mechanism switches to accretion at a metallicity level referred to as the critical metallicity of accretion, since the abundance of the small grains formed by shattering becomes large enough to rapidly increase the grain abundance by accretion. Just after the system has reached this stage, the small-to-large grain abundance ratio reaches the maximum. After that, this ratio converges to the value determined by the balance between shattering and coagulation, and the dust-to-metal ratio is determined by the balance between accretion and shock destruction.

With a Monte Carlo simulation, we showed that the simplicity of our model has an advantage in predicting statistical properties. We also demonstrated that our two-size approximation is also useful in predicting observational dust properties such as extinction curves. In our future work, we will incorporate the formulation developed in this paper into cosmological galaxy formation and evolution models.

ACKNOWLEDGMENTS

We thank R. Schneider for careful reading and helpful comments. We are grateful to A. Rémy-Ruyer for providing us with the nearby galaxy data of dust-to-gas ratio and metallicity, and to Y.-H. Chu, K.-C. Hou, and the interstellar and circumstellar group in our institute for useful comments. We thank the support from the Ministry of Science and Technology (MoST) grant 102-2119-M-001-006-MY3.

REFERENCES

- Amari, S., Lewis, R. S., & Anders, E. 1994, *Geochim. Cosmochim. Acta*, 58, 459
- Anders, E., & Grevesse, N. 1989, *Geochim. Cosmochim. Acta*, 53, 197
- Asano, R., Takeuchi, T. T., Hirashita, H., & Nozawa, T. 2013a, *MNRAS*, 432, 637 (A13)
- Asano, R., Takeuchi, T. T., Hirashita, H., & Inoue, A. K. 2013b, *Earth Planets Space*, 65, 213
- Asano, R., Takeuchi, T. T., Hirashita, H., & Nozawa, T. 2014, *MNRAS*, 440, 134
- Bekki K., 2013, *MNRAS*, 432, 2298
- Bianchi R., Schneider R., 2007, *MNRAS*, 378, 973
- Bohren C. F., Huffman D. R., 1983, *Absorption and Scattering of Light by Small Particles*. Wiley, New York
- Cazaux, S., & Tielens, A. G. G. M. 2004, *ApJ*, 604, 222
- Daulton, T. L., et al. 2003, *Geochim. Cosmochim. Acta*, 67, 4743
- Dayal, P., Hirashita, H., & Ferrara, A. 2010, *MNRAS*, 403, 620
- de Bennassuti, M., Schneider, R., Valiante, R., & Salvadori, S. 2014, *MNRAS*, 445, 3039
- Désert, F.-X., Boulanger, F., & Puget, J. L. 1990, *A&A*, 237, 215
- Draine B. T., 2009, in Henning Th., Grün E., Steinacker J., eds, *ASP Conf. Ser. 414, Cosmic Dust – Near and Far*. Astron. Soc. Pac., San Francisco, p. 453
- Draine, B. T., & Anderson, N. 1985, *ApJ*, 292, 494
- Draine, B. T., & Salpeter, E. E. 1979b, *ApJ*, 231, 77
- Dwek, E. 1998, *ApJ*, 501, 643
- Dwek, E., & Scalo, J. M. 1980, *ApJ*, 239, 193
- Fitzpatrick, E. L., & Massa, D. 2007, *ApJ*, 663, 320
- Galametz, M., Madden, S. C., Galliano, F., Honny, S., Bendo, G. J., & Sauvage, M. 2011, *A&A*, 532, A56
- Galliano, F., et al. 2011, *A&A*, 536, 88
- Gall, C., Hjorth, J., & Andersen, A. C. 2011, *A&AR*, 19, 43
- Gauger, A., Balega, Y. Y., Irrgang, P., Osterbart R., & Weigelt G. 1999, *A&A*, 346, 505
- Gould, R. J., & Salpeter, E. E., 1963, *ApJ*, 138, 393
- Groenewegen, M. A. T. 1997, *A&A*, 317, 503
- Hirashita, H. 1999, *ApJ*, 510, L99
- Hirashita, H. 2012, *MNRAS*, 422, 1263
- Hirashita, H., & Ferrara, A. 2002, *MNRAS*, 337, 921
- Hirashita, H., & Kuo, T.-M. 2011, *MNRAS*, 416, 1340

Hirashita, H. & Voshchinnikov, N. V. 2014, MNRAS, 437, 1636
 Hirashita, H. & Yan, H. 2009, MNRAS, 394, 1061
 Hofmann, K.-H., Balega, Y., Blöcker, T., & Weigelt, G. 2001, A&A, 379, 529
 Hoppe, P., Amari, S., Zinner, E., Ireland, T., & Lewis, R. S. 1994, ApJ, 430, 870
 Hoppe, P., & Zinner, E. 2000, J. Geophys. Res., 105, 10371
 Inoue, A. K. 2003, PASJ, 55, 901
 Inoue, A. K. 2011, Earth, Planets Space, 63, 1027
 Jones, A. P., & Nuth, J. A., III 2011, A&A, 530, A44
 Jones, A. P., Tielens, A. G. G. M., & Hollenbach, D. J. 1996, ApJ, 469, 740
 Kennicutt, R. C., et al. 2011, PASP, 123, 1347
 Kimura, H., Mann, I., & Jessberger, E. K. 2003, ApJ, 583, 314
 Kuo, T.-M. & Hirashita, H. 2012, MNRAS, 424, L34
 Kuo, T.-M., Hirashita, H., & Zafar, T. 2013, MNRAS, 436, 1238
 Li, A., & Draine, B. T. 2001, ApJ, 554, 778
 Lisenfeld, U., & Ferrara, A. 1998, ApJ, 496, 145
 Madden, S. C., et al. 2013, PASP, 125, 600
 Mathis, J. S., Rumpl, W., & Nordsieck, K. H. 1977, ApJ, 217, 425 (MRN)
 Mattsson, L. 2011, MNRAS, 414, 781
 Mattsson, L., De Cia, A., Andersen, A. C., Zafar, T. 2014, MNRAS, 440, 1562
 McKee, C. F. 1989, in Allamandola L. J. & Tielens A. G. G. M. eds., IAU Symp. 135, Interstellar Dust, Kluwer, Dordrecht, 431
 Michałowski, M. J., Murphy, E. J., Hjorth, J., Watson, D., Gall, C., & Dunlop, J. S. 2010, A&A, 522, A15
 Nozawa, T., Asano, R. S., Hirashita, H., & Takeuchi, T. T. 2015, MNRAS, 447, L16
 Nozawa, T., & Fukugita, M. 2013, ApJ, 770, 27
 Nozawa, T., Kozasa, T., & Habe, A. 2006, ApJ, 648, 435
 Nozawa, T., Kozasa, T., Habe, A., Dwek, E., Umeda, H., Tomimaga, N., Maeda, K., & Nomoto, K. 2007, ApJ, 666, 955
 Omukai, K. 2000, ApJ, 534, 809
 Omukai, K., Tsuribe, T., Schneider, R., & Ferrara, A. 2005, ApJ, 626, 627
 Ormel, C. W., Paszun, D., Dominik, C., & Tielens, A. G. G. M. 2009, A&A, 502, 845
 Pei, Y. C. 1992, ApJ, 395, 130
 Pipino, A., et al. 2011, A&A, 525, A61
 Rémy-Ruyer, A., et al. 2013, A&A, 557, A95
 Rémy-Ruyer, A., et al. 2014, A&A, 563, A31
 Rowlands, K., Gomez, H. L., Dunne, L., Aragón-Salamanca, A., Dye, S., Maddox, S., da Cunha, E., & van der Werf, P. 2014, MNRAS, 441, 1040
 Schneider, R., Omukai, K., Inoue, A. K., & Ferrara, A. 2006, MNRAS, 369, 1437
 Schneider, R., Valiante, R., Ventura, P., dell'Agli, F., Di Crescenzo, M., Hirashita, H., & Kemper, F. 2014, MNRAS, 442, 1440
 Seok, J. Y., Hirashita, H., & Asano, R. S. 2014, MNRAS, 439, 2186
 Takeuchi, T. T., Ishii, T. T., Nozawa, T., Kozasa, T., & Hirashita, H. 2005, MNRAS, 362, 592
 Tinsley, B. M. 1980, Fundamentals of Cosmic Physics, 5, 287
 Valiante, R., Schneider, R., Salvadori, S., & Bianchi, S. 2011, MNRAS, 416, 1916
 Ventura, P., et al. 2012, MNRAS, 424, 2345
 Weingartner, J. C., & Draine, B. T. 2001, ApJ, 548, 296
 Winters, J. M., Fleischer, A. J., Le Bertre, T., & Sedlmayr, E. 1997, A&A, 326, 305

Yajima, H., Nagamine, K., Thompson, R., & Choi, J.-H. 2014, MNRAS, 439, 3073
 Yan, H., Lazarian, A., & Draine, B. T. 2004, ApJ, 616, 895
 Yasuda, Y., & Kozasa, T. 2012, ApJ, 745, 159
 Yozin C., Bekki, K., 2014, MNRAS, 443, 522
 Zhukovska S., 2014, A&A, 562, A76
 Zhukovska S., Gail H.-P., Tieloff M., 2008, A&A, 479, 453
 Zhukovska S., Henning T. 2013, A&A, 555, A99

APPENDIX A: TEST FOR THE LOGNORMAL MODEL

We examine how well the Milky Way extinction curve is reproduced by the log-normal model of grain size distribution (equation 30), comparing it with the Mathis et al. (1977) (MRN) grain size distribution ($\propto a^{-3.5}$ in the grain radius range of 0.001–0.25 μm), which is already known to reproduce the Milky Way extinction curve well. The mass ratio of silicate to carbonaceous dust is assumed to be the same as the value used in the text (0.54 : 0.46). We adopt the same small-to-large grain abundance ratio as the MRN model (0.30 : 0.70; see section 2.2); that is, we do not use the output of our dust enrichment model for the purpose of simply comparing with the MRN model.

In Fig. A1, we compare the grain size distributions and the extinction curves. Although the lognormal model deviates from the observed mean extinction curve of the Milky Way more than the MRN model, the difference between these two models is significant only at the bump around $\sim 0.22 \mu\text{m}$ contributed from small graphite grains and toward far-ultraviolet wavelengths, and the deviations are within 20 per cent. We expect that, in calculating extinction curves in extragalactic objects, the uncertainties arising from assumed grain properties are rather larger. Therefore, we conclude that the simple lognormal model provides a good approximate method of calculating extinction curves based on the two-size approximation.

This paper has been typeset from a $\text{\TeX}/\text{\LaTeX}$ file prepared by the author.

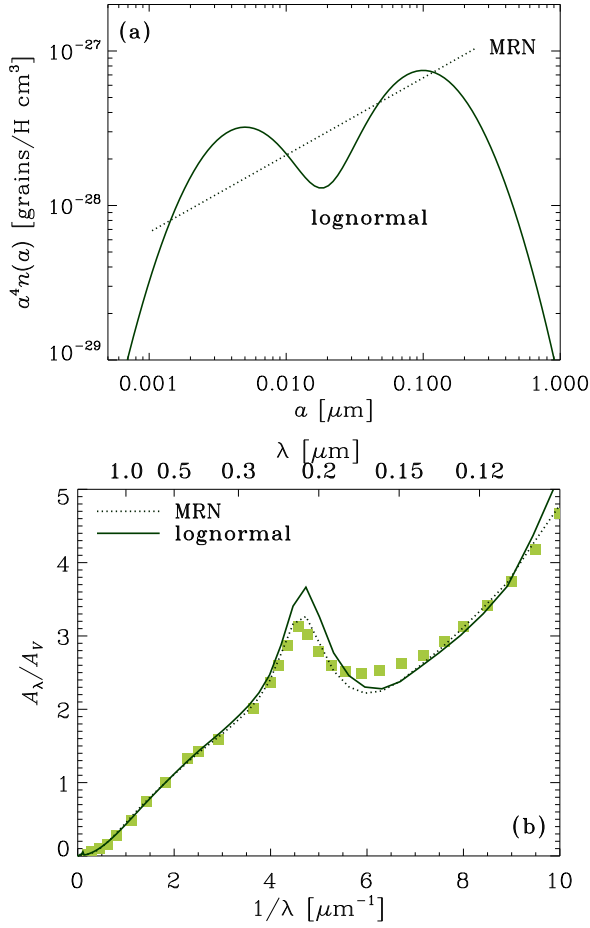


Figure A1. (a) Comparison between the two grain size distribution models (MRN and lognormal models) with the same small-to-large grain abundance ratio. The grain size distributions are presented by multiplying a^4 to show the mass distribution in each logarithmic bin of the grain radius a . (b) Extinction curves calculated with the lognormal and MRN models (solid and dotted lines, respectively). The extinction is normalized to the value at the V band ($0.55 \mu\text{m}$). The filled squares are the observed mean extinction curve of the Milky Way taken from Pei (1992).